Modeling and Measured Verification of Stored Energy and Loss in MEMS Toroidal Inductors

Mohammad Araghchini, Jeffrey H. Lang
Massachusetts Institute of Technology
Cambridge, USA
Email: mohamad@mit.edu

Xuehong Yu, Min Soo Kim,
Florian Herrault, Mark G. Allen
Georgia Institute of Technology
Atlanta, USA

Jizheng Qiu, Charles R. Sullivan
Dartmouth University
Hanover, USA

***Abstract*—This paper presents the derivation and verification of a sinusoidal-steady-state equivalent-circuit model for microfabricated inductors developed for use in integrated power electronics. These inductors have a low profile, a toroidal air core, and a single-layer winding fabricated via high-aspect-ratio molding and electroplating. Such inductors inevitably have a significant gap between winding turns. This makes the equivalent resistance more difficult to model. The low profile increases the significance of energy stored in the winding which, together with the winding gap, makes the equivalent inductance more difficult to model as well. The models presented here account for these effects. Finally, the models are verified against results from 2D FEA, 3D FEA, direct measurement, and in-circuit experimentation. In all cases, the equivalent-circuit model is observed to be accurate to within several percent.**

I. Introduction

Passives, namely inductors, transformers and capacitors, are often the largest and most expensive components in power electronic circuits. Further, the magnetics (inductors and transformers) are often responsible for a large portion of the power loss. As operating frequencies are increased, the physical size of the passives can, in theory, be reduced while maintaining or improving efficiency [1]. Realizing this reduction in size and simultaneous improvement in efficiency requires improvements in magnetics technology.

As the switching frequencies of the power electronics rise and the size of the magnetics falls, new fabrication strategies for the magnetics, such as MEMS microfabrication, become possible. On-chip inductors built for power converters in the multi-megahertz range using MEMS-like microfabrication include [2]–[12] and are reviewed in [13]. With sufficiently small volume, the magnetics can be embedded in the substrate of the power circuit or within a secondary substrate and flip-bonded above the power circuit. If the inductor is embedded in the power-circuit substrate, the dead space of the substrate is then used for magnetics, eliminating the high profile of the magnetics and greatly reducing the volume of the system.

Air-core magnetics offer the advantages of avoiding magnetic core losses and avoiding fabrication processes that incorporate special materials [1], [14], [15]. While planar spiral and solenoidal air-core inductors produce significant external fields which may cause electromagnetic interference problems and losses in nearby conductors, toroidal inductors need not. Microfabricated toroidal inductors have been fabricated above substrates [16]–[19], as well as embedded in substrates. The most common embedding is in printed circuit boards in which toroidal magnetics are formed using copper traces and plated-through vias [20], [21]. However, toroidal microfabricated inductors have also been embedded in silicon and other substrates [22], [23]. The development of embedded toroidal air-core inductors related to this paper is presented in [24].

The focus of this paper is equivalent circuit models that can support the analysis, optimization and design of MEMS-microfabricated toroidal air-core inductors of the type described in [24]. To that end, the remainder of this paper is organized as follows. Section II presents geometric and magnetic details of the inductors considered here. Section III presents the models that are a main focus of this paper. These include models for electromagnetic fields, and their abstraction into an equivalent-circuit model. Section IV briefly describes the MEMS fabrication of inductors that support experimental verification of the models. Section V presents model verification based on the results of both numerical and physical experiments. Finally, Section VI summarizes this paper and offers concluding remarks.

II. Toroidal Inductors

Toroidal inductors provide a compact means for storing energy. They are amenable to having a large number of turns, and hence a high inductance, and they have largely self-contained magnetic flux. The style of toroidal inductor considered here is shown in Fig. 1(a). It is a single-layer air-core inductor microfabricated on/in a lossless substrate that can be flip-bonded to a power-electronic circuit.

Microfabrication of the inductors considered here relies on high-aspect-ratio molding and electroplating to form 3D copper windings with near-mm-tall vertical conductors [24]. The inductor shown in Fig. 1(a), for example, has 25 turns with a 100-μm gap between turns, a 650-μm height, and inner and outer radii of 1 mm and 3 mm, respectively. The copper winding is approximately 30 μm thick over all surfaces. Further fabrication details are discussed in Section IV.

As seen in Fig. 1(a), the inductor winding spirals around the toroid in the poloidal direction as the spiral progresses in the toroidal direction. Thus there exists a single-turn toroidal

This research project is sponsored by ARPA-E under Award Number DE-AR0000123.

978-1-4673-0803-8/12/$31.00 ©2012 IEEE

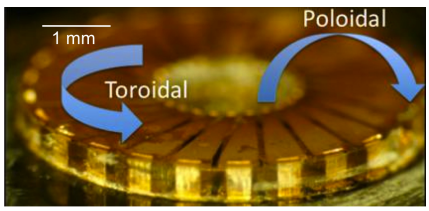

(a) Microfabricated and functional inductor.

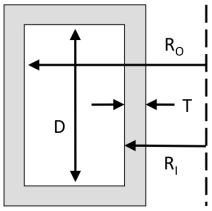

(b) Inductor dimensions used during modeling.

Fig. 1. Toroidal inductor and dimensions used during its modeling.

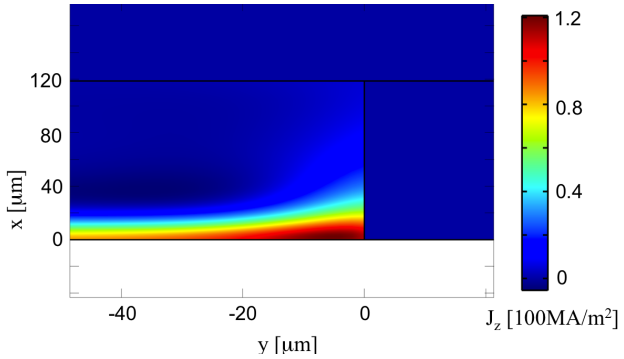

Fig. 2. An example of finite-element simulation for toroidal windings. Shown is one section of a periodic multi-turn structure with side-by-side turns, simulated by the use of symmetry boundary conditions at the left and right of this section.

current and a multi-turn poloidal current. At low frequencies, these currents occupy the entire winding volume, and create a net current that follows the winding. However, at high frequencies these currents are forced to the winding surface through magnetic diffusion. The poloidal current terminates the toroidal magnetic flux that travels around the interior toroid core, and thus flows on the inner winding surface. The toroidal current terminates the exterior poloidal magnetic flux that passes through the center hole of the toroid, and thus flows on the outer winding surface. When either current meets the edge of a winding turn, it flows down that edge and becomes the other current on the opposite side. Because the two currents are orthogonal, their associated energy storage and losses can be computed independently at all frequencies. In practice, for a toroid wound with many turns, the poloidal current density is much larger than the toroidal current density. Since the two currents occupy the same total volume at all frequencies the stored magnetic energy and losses associated with the poloidal current are generally much greater.

For modeling purpose, several dimensions are defined as shown in Fig. 1(b). The inductor is assumed to have a toroidal core with a square cross section. This cross section has inner and outer radii R_{I} and R_{O}, respectively, and height D. The thickness of the winding wrapped around the core is T. The number of turns in the winding is N, and the gap between turns is G, independent of radius.

III. Modeling

The models presented here begin with the electromagnetic fields within the inductor and proceed to an equivalent circuit model extracted from those fields. The equivalent circuit model captures both stored energy and loss. For inductors of the type shown in Fig. 1(a), it is the losses that are the more difficult to model because they depend strongly on the details of magnetic fields at the winding surface while these fields store only a fraction of the energy.

The inductors considered here carry a single-layer multi-turn winding that is thick compared to a skin depth during typical AC operation. The added thickness is chosen based on DC operating considerations. A simple AC model of such a winding would consider currents flowing within one skin depth of the winding surface. However, as seen in Fig. 2, the currents are not uniform across the surface. Rather, the gaps between winding turns cause the currents to concentrate at the corners, and flow on the sides, of each turn [15]. With wide gaps, greater than several skin depths, this results in a significant increase in losses that is captured only by improved models. One such set of models is presented here.

A. Energy Methods

The foundational models presented below are derived with the same energy methods [25] that underlie finite-element analysis (FEA) [26]. FEA typically segments space into many small regions, and expresses a potential over each region by a simple function having a few free parameters. The potential is then used to determine the energy stored in each region, and the individual stored energies are summed to obtain a total. Finally, the values of the free parameters are determined numerically by minimizing the total stored energy over those parameters. The resulting potentials can then be used for subsequent numerical analyses, such as the determination of equivalent circuit models and so on. In contrast, the approach taken here employs a few potential functions that are valid over large regions of an inductor, each having again a few free parameters. Moreover, the determination and minimization of stored energy is done analytically, so that all subsequent analyses can remain analytical as opposed to becoming numerical. This results in analytic expressions for the equivalent circuit models that can be examined for physical insight and rapidly evaluated during iterative design optimization. Such an approach has been used to analyze the magnetic [27] and thermal [28] behavior of electric machines.

B. Air Fields

The first modeling step is to determine the toroidal magnetic fields inside the inductor core, and the poloidal magnetic fields outside the inductor. Since these fields will be used to determine boundary conditions for loss calculations, they must include the effects of the gaps between winding turns as argued from Fig. 2. Here, the winding is assumed to be perfectly conducting, and the energy method discussed Section III-A is employed over three steps. First, the two spaces are segmented into a few small regions, and functions are selected for the magnetic vector potential A in each region. Following [25] the

only constraints on the functions are that they be continuous from region to region, and that the associated magnetic fields be parallel to the surfaces of the perfectly-conducting winding. Next, the magnetic field in each region is determined from its vector potential and used to determine the stored magnetic energy in that region. Finally, the total stored magnetic energy is minimized to determine any free parameters included in the original vector potentials. The resulting magnetic field can then be used to determine winding inductance, surface currents, and losses as discussed in Subsection III-C.

Consider first the toroidal field inside the core shown in Fig. 3. This figure is a Cartesian approximation to the actual circular geometry. This core is divided into three regions having a common origin. Because the poloidal currents, J_z in the figure are $\hat{z}$-directed, the vector potential is too. Correspondingly, the vector potentials are selected to be

$$A_{z1} = -\frac{2x}{D} + C_1 \sin\left(\frac{\pi 2x}{D}\right) e^{\beta_y y} \tag{1}$$

$$\begin{aligned} A_{z2} &= -\frac{2x}{D} + \left(1+\frac{2x}{D}\right) C_3 \sin\left(\frac{\pi y}{G}\right) \\ &\quad + C_1 \sin\left(\frac{2\pi x}{D}\right)\left(1 + C_2 \sin\left(\frac{\pi y}{G}\right)\right) \end{aligned} \tag{2}$$

$$A_{z3} = C_3 \sin\left(\frac{\pi y}{G}\right) e^{-\beta_x x} \tag{3}$$

where C_1, C_2, C_3, β_y and β_x are free parameters. In each region the magnetic field, $\bar{H}$ is given by

$$\mu_\circ \bar{H} = \nabla \times \bar{A} \quad . \tag{4}$$

Using this magnetic field, the total stored magnetic energy E is determined from

$$E = \int \frac{\mu_0}{2} |H|^2 \, dV \tag{5}$$

as a function of the free parameters where the integral is taken over Region 1, and the left half of Regions 2 and 3. Finally, by minimizing E, the free parameters are determined as functions of the geometric and physical parameters of the inductor. Thus, the free parameters become

$$C_1 = -12G^3D^2/(\pi M) \quad , \quad C_2 = (\pi G - D)/(2G) \tag{6}$$

$$C_3 = \frac{12G^2\left(\pi(G^2+\frac{1}{4}D^2)(\pi G - D) - 8G^3\right)}{\pi M} \tag{7}$$

$$\beta_x = \pi/G \quad , \quad \beta_y = -2\pi/D \tag{8}$$

where

$$\begin{aligned} M &= \frac{\pi F^2 G^2}{8}\left(G\left(2\pi^3 - 22\pi\right) + F\left(-6+\pi^2\right)\right) \\ &\quad + \frac{\pi FG}{16}\left(\left(F^3\left(\pi^3 - 12\pi\right)\right) + G^3\left(24\pi^2 - 240\right)\right) \\ &\quad - \frac{\pi F^5}{16}\left(-6+\pi^2\right) + 3G^5\left(-8+\pi^2\right) \end{aligned} \tag{9}$$

In the analysis above, one approximation must be noted. In (5) it is assumed that β_x and β_y are large enough to permit the integration of the exponential terms to infinity. This is observed to be the case through FEA for typical geometries.

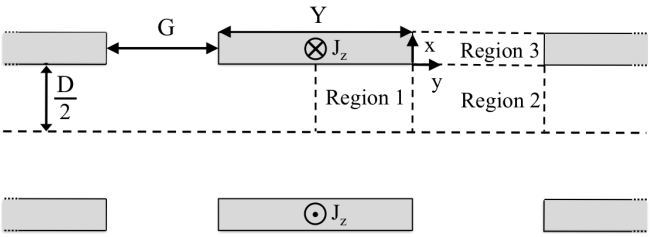

Fig. 3. A schematic of the toroidal core as viewed from the edge of the inductor looking into the figure in the direction of radial current flow. One full and two partial winding turns are visible in this view.

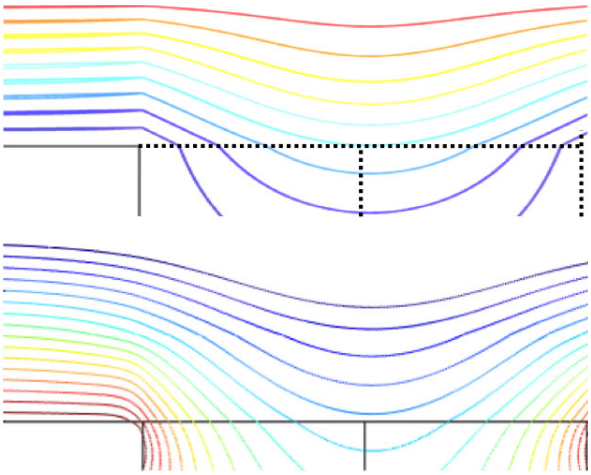

Fig. 4. Magnetic field lines in the gap between two adjacent windings in a toroidal inductor as plotted by the analytical model calculation (top) and by a COMSOL numerical simulation (bottom).

To illustrate the results derived above, Fig. 4 plots the $\bar{H}$ lines derived from (4) and an FEA simulation for a sample inductor. As observed in the figure, the $\bar{H}$ lines from the analytical model are similar to the $\bar{H}$ lines computed by FEA.

In Fig. 5 the space outside the inductor is divided into five regions. As for toroidal fields in the core, simple magnetic vector potentials for these regions are selected with free parameters to be optimized. For simplicity, we provide here only the magnetic vector potentials because the expressions that follow are long. These expressions are determined by Maple [29] and evaluated directly with MatLab [30] mainly without human intervention. The vector potentials in the five regions are selected to be

$$A_{\phi 1} = \frac{A_0 \rho}{R_{\rm I}} \ , \ A_{\phi 2} = \frac{A_0 \rho}{R_{\rm I}} \left(\frac{\frac{D}{2}+T}{z}\right)^n \ , \ A_{\phi 5} = \frac{A_0 R_{\rm O} R_{\rm I}}{\rho^2} \tag{10}$$

$$A_{\phi 3} = \frac{A_0 R_I}{\rho} \left(\frac{\frac{D}{2}+T}{z}\right)^n \ , \ A_{\phi 4} = \frac{A_0 R_{\rm O} R_{\rm I}}{\rho^2} \left(\frac{\frac{D}{2}+T}{z}\right)^n \tag{11}$$

where n is a free parameter and A_0 is a normalization factor.

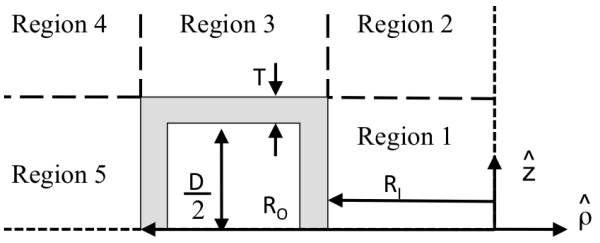

Fig. 5. A schematic of upper half of the toroidal inductor cross section. We have cylindrical symmetry around z axis.

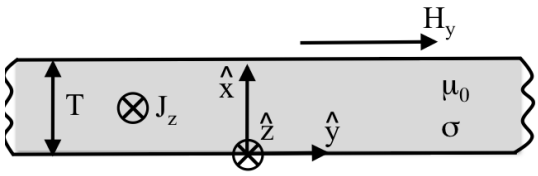

Fig. 6. Conductor geometry for magnetic diffusion analysis.

C. Winding Fields

In Subsection III-B it was assumed that the winding was perfectly conducting. Based on this assumption, the magnetic fields in the air regions of the inductor were determined. In contrast, this section focuses on the fields in the winding, and ultimately on the energy stored and losses in the winding, when its conductors are imperfect.

The analysis presented here is perturbational in the sense that it is assumes that the analysis of Subsection III-B still holds even though the winding is no longer a perfect conductor. In other words, the winding is still sufficiently perfectly conducting to justify the analysis of Subsection III-B. In this case, the magnetic fields determined in Subsection III-B provide boundary conditions for a magnetic-diffusion analysis of the winding. This analysis begins with Fig. 6 which shows the edge view of a winding of thickness T, conductivity σ and free-space permeability $\mu_\circ$. The conductor carries a current density J_z in the $\hat{z}$ direction. This current density terminates the $\hat{y}$-directed magnetic field H_y that exists just outside the conductor at $x = T$. By $x = 0$, the magnetic field is fully terminated by J_z, and hence vanishes.

Following [31] and [32], with the boundary conditions described above, the magnetic field inside the winding is

$$H_y = \Re\left\{H_\circ \frac{\sinh(\alpha x)}{\sinh(\alpha T)} e^{j\omega t}\right\} \quad , \tag{12}$$

and the current density inside the conductor is

$$J_z = \Re\left\{\alpha H_\circ \frac{\cosh(\alpha x)}{\sinh(\alpha T)} e^{j\omega t}\right\} \quad , \tag{13}$$

where $H_\circ$ is the peak magnetic field at $x = T$, ω is the temporal frequency of that magnetic field, and

$$\alpha = (1+j)/\delta \quad , \quad \delta = \sqrt{2/\omega\mu_\circ\sigma} \quad . \tag{14}$$

The magnetic field and current density can now be used to determine the time-average magnetic stored energy density $\langle W\rangle$ and the time-average dissipated power density $\langle P\rangle$ in the winding as follows. The stored magnetic energy density is

$$\begin{aligned}\langle W\rangle &= \int_0^T \frac{\mu_\circ}{4}|H_y|^2 dx \\ &= \frac{\mu_\circ H_\circ^2 \delta}{8} \frac{\sinh(2T/\delta)-\sin(2T/\delta)}{\cosh(2T/\delta)-\cos(2T/\delta)} \quad , \end{aligned} \tag{15}$$

and the dissipated power density is

$$\begin{aligned}\langle P\rangle &= \int_0^T \frac{1}{2\sigma}|J_z|^2 dx \\ &= \frac{H_\circ^2}{2\sigma\delta} \frac{\sinh(2T/\delta)-\sin(2T/\delta)}{\cosh(2T/\delta)-\cos(2T/\delta)} \quad . \end{aligned} \tag{16}$$

The two densities are surface densities in the y-z plane. Equations (15) and (16), together with the formulation of Section III-B, represent a departure from the traditional method of modeling winding phenomena that rely on curve fitting [15] or Wheeler's formula [16].

As noted in Section II, the inductor winding terminates a toroidal magnetic field on one side and a poloidal magnetic field on the other. Thus both orientations of magnetic field and current density exist in all conductors. Because the two magnetic fields are spatially orthogonal, and the two current densities are spatially orthogonal, their cross products are not present in the generalization of (15) and (16). Therefore, (15) and (16) may be used twice to determine the stored magnetic energy and loss for each conductor, once for toroidal magnetic fields and poloidal currents, and once for the poloidal magnetic fields and toroidal currents.

D. Equivalent Circuit

This subsection develops an equivalent-circuit inductor model for sinusoidal steady-state operation. Such models are useful because they capture what is naturally measured during a characterization experiment, namely inductor impedance as a function of frequency. They are also useful for power circuit co-optimization and design during steady-state operation. Here, the model is presented as a series inductance L and resistance R as functions of frequency.

Consider first the inductance, which represents energy storage in the inductor. The four components of this inductance are those associated with magnetic energy stored in the toroidal fields inside the air core and the winding, and those associated with magnetic energy stored in the poloidal fields outside the inductor and inside the winding.

For the purposes of computing stored energy, the toroidal magnetic fields inside the inductor may be assumed to follow concentric closed circular paths. This leads to the traditional inductance L_{AT} for a toroidal air core inductor given by [33]

$$L_{AT} = \frac{\mu_\circ N^2 D}{2\pi} \ln(R_O/R_I) \quad . \tag{17}$$

Alternatively, the magnetic fields from Subsection III-B can be used to determine L_{AT}. However, experience shows that the two inductances are nearly equal except for short inductors with large winding gaps, that is, with small D and large G.

Given the simplicity of (17), it is adopted here.

The poloidal magnetic fields outside the inductor are not as easily modeled as those inside the inductor. However, experience [15] shows that treating the inductor as a single turn wire loop following [34] or [35] yields a useful approximation to the poloidal-field inductance given by

$$L_{AP} = \frac{\mu_\circ (R_O + R_I)}{2}\left(\ln\left(\frac{8(R_O+R_I)}{(R_O-R_I)}\right) - 2\right) \quad . \tag{18}$$

Again, the magnetic fields from Subsection III-B can be used to determine L_{AP}. However, given the simplicity of (18) it too is adopted here.

To determine the inductances associate with magnetic energy stored in the toroidal and poloidal fields in the winding, (15) is integrated over the corresponding winding surfaces and equated to the corresponding time-average stored magnetic energies written in terms of the inductances. This yields

$$\frac{1}{4} L_{WT} I_\circ^2 = \int_{S_{zP}} \int_{S_{yP}} \langle W \rangle \; dy \; dz \tag{19}$$

$$\frac{1}{4} L_{WP} I_\circ^2 = \int_{S_{zT}} \int_{S_{zT}} \langle W \rangle \; dy \; dz \tag{20}$$

where $I_\circ$ is the peak current at the inductor terminals. In (19), S_{yP} and S_{zP} denote the $\hat{y}$-directed lateral span and the $\hat{z}$-directed path, respectively, of the winding as it carries the poloidal currents on its inner surface. S_{yP} is extended to $x = \infty$ in Region 3 in Fig. 3. In (20), S_{yT} and S_{zT} denote the $\hat{y}$-directed lateral span and the $\hat{z}$-directed path, respectively, of the winding as it carries the toroidal currents on its outer surface. S_{yT} includes the surfaces in Regions 1, 3 and 5 in Fig. 5. In both cases, $\hat{y}$ and $\hat{z}$ refer to the transverse and longitudinal directions in Fig. 6. Both (19) and (20) involve (15), and hence $H_\circ$. There, $H_\circ$ is the peak magnetic field evaluated at the corresponding winding surface as developed in Subsection III-B. Finally, $I_\circ$ is obtained by integrating the $\hat{z}$-directed surface current, which is equivalent to H_y from Subsection III-B, over either winding surface according to

$$I_\circ = \int_{S_{yT}} H_\circ \; dy = \int_{S_{yP}} H_\circ \; dy \quad . \tag{21}$$

The complete inductance is

$$L = L_{AT} + L_{AP} + L_{WT} + L_{WP} \quad . \tag{22}$$

The four inductance terms are placed in series in (22) because their stored energies are driven by the same terminal current.

To determine the resistances associated with loss in the winding, (16) is integrated over the corresponding winding surfaces and equated to the corresponding time-average power dissipation written in terms of the resistances. This results in

$$\frac{1}{2} R_{WT} I_\circ^2 = \int_{S_{zP}} \int_{S_{yP}} \langle P \rangle \; dy \; dz \tag{23}$$

$$\frac{1}{2} R_{WP} I_\circ^2 = \int_{S_{zT}} \int_{S_{zT}} \langle P \rangle \; dy \; dz \quad . \tag{24}$$

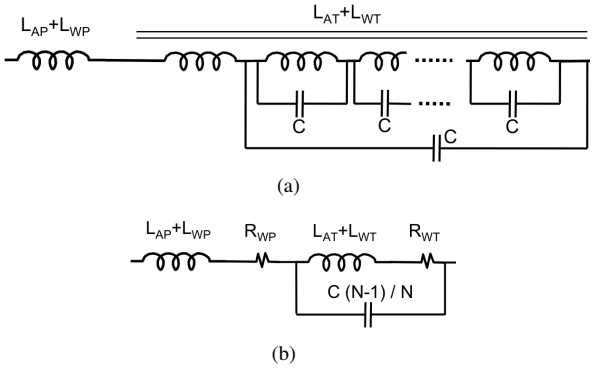

Fig. 7. Semi-distributed model for estimating self resonance frequency (a) and reduced circuit model (b).

The complete resistance is

$$R = R_{WT} + R_{WP} \quad . \tag{25}$$

The individual resistances in (25) are again placed in series because their losses are driven by the same terminal current. For the same reason, R belongs in series with L.

It is important to observe that (19), (20), (21), (23) and (24) all involve the same approximation. In particular, (15) and (16) are developed for a conductor assuming uniform fields over y and z. That is, H_y at the winding surface is uniform in Fig. 6. Yet, as observed in Fig. 2 and developed in Subsection III-B, H_y at the winding surface, as represented by $H_\circ$ in (15) and (16), is not uniform. This three-dimensional character of the magnetic diffusion is ignored, and $H_\circ$ as used in (15), (16) and (21) is taken to be a function of y and z for the purposes of integration in (19), (20), (21), (23) and (24).

E. Parasitic Capacitance & Self Resonance

Parasitic capacitance between turns, and the self resonance that it creates, limits the performance of an inductor and degrades Q in high-frequency integrated power electronics. Thus, it is useful to estimate the self-resonance frequency. This is accomplished with the semi-distributed model shown in Fig. III-E(a), appropriate for an inductor fabricated on/in an insulating substrate. In this model, the inductor is treated as a leakage-free multi-winding transformer with one transformer winding per inductor turn, and a parasitic capacitor between each pair of neighboring inductor turns. Given the geometry of the inductors, the magnetic energy stored in the transformer is only that associated with L_{AT} and L_{WT}. Analysis of the distributed circuit shows that it is equivalent to L_{AT} and L_{WT} in parallel with a single capacitor having capacitance $C(N-1)/N$. This leads to the expanded equivalent circuit shown in Fig. III-E(b).

IV. Fabrication

To minimize substrate losses, the inductors considered here are assumed to be microfabricated on/in insulating substrates. The experimental inductors reported in Section V were fabricated in SU-8 molds on glass substrates. Their fabrication details are

most similar to those reported in [24], though the inductors in [24] were embedded in conducting silicon substrates.

The microfabrication of toroidal air-core inductors employs high-aspect-ratio molding and electroplating to form a three-dimensional copper winding. A key step is the fabrication of high-aspect-ratio near-mm-tall SU-8 vias filled with electroplated copper. This fabrication process relies on multiple steps of copper electroplating through photoresist molds. First, the bottom copper conductors are electroplated through a removable mold. A thick SU-8 mold is then weight-casted and lithographically patterned to create high-aspect-ratio vias. Using a mesh seed layer evaporated at the start of the process, the vertical conductors are electroplated through these 0.5-mm-tall vias. A spray coating technique is then utilized to create the mold for the electrodeposition of the top conductors. After conductor fabrication and mold removal, the mesh seed layer is etched away to individually isolate the turns, resulting in three-dimensional microfabricated toroidal inductors. Inductors microfabricated by the process described above, and tested in Section V, are generally characterized by a cavity height D up to 0.5 mm, a conductor thickness T up to 30 μm, a winding gap G down to 100 μm, and a minimum conductor width at the inner radius R_I down to 80 μm.

V. Model Verification

This section compares the inductance and resistance predicted by the models presented in Section III to those calculated by FEA and those measured through experiment.

A. Finite Element Analysis

Table I presents a comparison between the winding loss model discussed in Section III and 2D FEA simulation for nine cases. Each case has a different combination of winding width (Y) and winding thickness (T); δ denotes the winding skin depth. For each combination of Y and T, the gap G between turns is 100 μm. The modeled loss is based upon a y-only integration of (23). Table I also presents an equivalent loss density based on a skin-depth (SD) model in which the winding currents are uniformly distributed in the $\hat{y}$ direction over the surface of a turn. The skin-depth model does not properly account for current crowding at the winding corners near the gaps between turns, nor for currents along the edges. This could lead to either an over estimate of losses, or an under estimate, depending on geometry. For each combination the table gives the losses in one turn per meter length as computed using COMSOL FEA, the model based upon (23), and the skin-depth model. The table also presents the percentage errors in both models relative to the FEA simulation. The table shows that the analytic model provides a much better match to the COMSOL FEA than does the skin-depth model.

Table II presents a comparison between the winding loss model discussed in Section III and 3D FEA simulation also for nine cases. The table presents the resistance extracted from FEA, the modeled resistance from (25), and a resistance based on a skin-depth model. The model from Section III exhibits errors in resistance of less than 3.5%, whereas the skin depth model has errors as high as 24%.

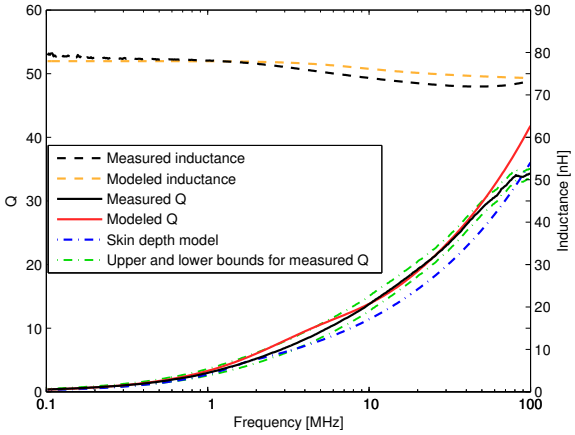

Fig. 8. Comparison between measured and modeled inductance and quality factor.

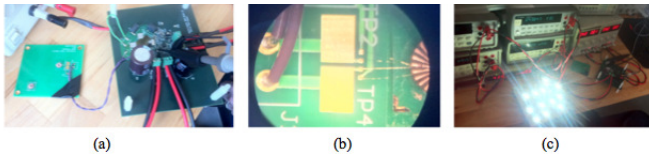

Fig. 9. Photographs of: (a) a micro-fabricated inductor bonded to a test board which is then connected to the ZVS converter; (b) a magnification of the bonding using gold wires; and (c) an LED driver demonstration.

B. Experimental Results

Fig. 8 shows the measured and modeled electrical characterization of a 650-μm-tall on-glass inductor fabricated with metal-encapsulated polymer vias [36]. The measurements were made by HP-4194 impedance analyzer. The modeled and measured inductance match well up to 100 MHz. The quality factor based on the models of Section III, shown by the solid red line, fits well within the measurement error bounds shown by dash-dot green lines, up to 30 MHz, while the simple skin-depth model under estimates the measured quality factor. Finally, a rough estimate of the parasitic capacitance C is 30 fF, which, from Figure III-E yields a resonance frequency near 3.5 GHz. This is well above the experimental frequencies in Fig. 8.

C. In-Circuit Measurements

This subsection examines the utility of the models developed here in predicting the performance of a microfabricated inductor in a power electronic circuit. An inductor was operated in a resonant zero-voltage-switching (ZVS) buck converter driving an LED load as shown in photographs in Fig. 9. Its inductance and resistance were extracted from experimental voltage and current measurements. Four experiments were performed in which the converter operated at different power levels. During each experiment the inductor voltage and current were recorded. Care was taken to compensate for the measurement delays of the oscilloscope channels to preserve accuracy.

The recorded voltage and current was processed to determine the inductance and resistance of the inductor. Table III

TABLE I
COMPARISON BETWEEN LOSS CALCULATIONS FROM 2D FEA, SECTION III AND THE SKIN-DEPTH MODEL. IN THIS TABLE, * INDICATES THAT THE CALCULATIONS ARE ACTUALLY PERFORMED FOR A WINDING THICKNESS OF $T = 4\delta$.

	$T = 3\delta$					$T = 10\delta$					$T = 50\delta$				
Y [μm]	2D FEA [W/m]	Analytic [W/m]	SD Loss [W/m]	SD Error [%]	Analytic Error [%]	2D FEA [W/m]	Analytic [W/m]	SD Loss [W/m]	SD Error [%]	Analytic Error [%]	2D FEA [W/m]	Analytic [W/m]	SD Loss [W/m]	SD Error [%]	Analytic Error [%]
100	4.82	5.10	7.0	31.7	5.4	4.55	4.4	7.0	34.5	-3.8	4.55	4.33	7.0	35.2	-4.9
300	2.02*	2.04*	2.3	14.2*	1.4*	1.99	1.96	2.3	24.4	-1.4	1.99	1.96	2.3	24.4	-1.9
1000	0.675	0.680	0.7	3.8	0.6	0.669	0.665	0.7	4.8	-0.6	0.67	0.66	0.7	4.6	-0.7

TABLE II
COMPARISON BETWEEN LOSS CALCULATIONS FROM 3D FEA, SECTION III AND THE SKIN-DEPTH MODEL.

Case	N	Frequency MHz	Gap G [μm]	Thickness T [μm]	Height [μm]	3D FEA [Ω]	Model [Ω]	SD [Ω]	Model Error	SD Error	Error Ratio: SD to Model
1	16	10	200	50	200	0.0516	0.0513	0.0566	-2.15	8.8	-4.1
2	16	20	200	50	200	0.0735	0.0725	0.0800	-1.05	8.1	-7.7
3	16	10	200	80	200	0.0492	0.0494	0.0564	0.52	12.8	24.5
4	16	10	200	80	1000	0.0765	0.0792	0.0894	3.52	14.4	4.1
5	32	10	150	50	200	0.198	0.1991	0.2425	-0.94	18.4	19.5
6	32	20	150	50	200	0.282	0.2815	0.3435	-0.02	17.7	-109.2
7	32	5	150	80	240	0.135	0.1361	0.1765	1.44	23.5	16.3
8	32	10	150	80	240	0.194	0.1939	0.2497	-0.07	22.3	343.6
9	32	20	150	80	240	0.275	0.2742	0.3531	-0.28	22.2	-79.7

summarizes the results of the four experiments. It shows a comparison between the inductance and resistance extracted from the experimental voltage and current measurements, modeled according to (22) and (25), and measured with the network analyzer. It also shows the resistances based upon the skin-depth method. The extracted, modeled and measured inductances and resistance agree well considering that the extracted parameters include an external wiring component. The resistance from the skin-depth model is consistently higher than the modeled and measured resistance.

VI. SUMMARY & CONCLUSIONS

This paper has presented the development and verification of a sinusoidal-steady-state equivalent-circuit model for microfabricated inductors intended for use in integrated power electronics. These inductors have a low profile, a toroidal air core, and a single-layer winding fabricated via high-aspect-ratio molding and electroplating. They are typically up to 1 mm tall and 1 cm in diameter, and are fabricated with windings having a thickness near 50 μm with a minimum feature size near 100 μm. Operating near 10 MHz, they could exhibit an inductance up to 700 nH and a quality factor up to 20.

The inductors considered here have a important gap between winding turns, greater than a few skin depths, due to fabrication limitations. This gap increases the losses and equivalent resistance by causing current crowding at the nearby winding edges. This makes the equivalent resistance more difficult to model. The low profile enhances the significance of magnetic energy stored in the winding, which, together with the winding gap, also makes the equivalent inductance more difficult to model. The models presented here account for these effects. The models begin with expressions for the magnetic fields in the air core and outside the inductor that are derived from a minimized stored energy formulation. These fields next serve as boundary conditions for a magnetic-diffusion analysis of the magnetic fields and current density in the winding. The resulting stored energy and losses throughout the inductor are summarized in a sinusoidal-steady-state equivalent-circuit model. To this model is added a parasitic capacitance to assist in the estimation of self resonance.

The models are verified against results from 2D FEA, 3D FEA, direct measurement and in-circuit experimentation. In all cases, the equivalent-circuit inductance and resistance is observed to be accurate to within several percent. Generally, the models perform best as the gap between the turns decreases relative to the turn width.

ACKNOWLEDGEMENTS

The authors gratefully thank J. Ranson and Prof. D. J. Perreault of MIT for assistance with experiments shown in Fig. 9.

REFERENCES

[1] D. Perreault, J. Hu, J. Rivas, Y. Han, O. Leitermann, R. Pilawa-Podgurski, A. Sagneri, and C. Sulivan, "Opportunities and challenges

TABLE III
IN-CIRCUIT EXPERIMENTAL RESULTS AND MODELING RESULTS FOR A MEMS MICROFABRICATED INDUCTOR IN A ZVS BUCK CONVERTER.

	Input Power [W]	Output Power [W]	Frequency [MHz]	Extracted L [nH]	Modeled L [nH]	Measured L [nH]	Extracted R [Ω]	Modeled R Ω	SD R [Ω]	Measured R [Ω]	Measured Q
Test1	6.4	5.7	9.26	101	95	94	0.47	0.382	0.465	0.377	14.5
Test2	4.4	3.8	9.56	101	95	94	0.54	0.389	0.473	0.378	14.8
Test3	2.5	2.1	9.61	101	95	94	0.58	0.389	0.473	0.378	14.8
Test4	1.3	0.9	9.58	101	95	94	0.50	0.389	0.473	0.378	14.8

in very high frequency power conversion," in *IEEE Applied Power Electronics Conference (APEC)*, feb. 2009, pp. 1 –14.

[2] Y. Fukuda, T. Inoue, T. Mizoguchi, S. Yatabe, and Y. Tachi, "Planar inductor with ferrite layers for dc-dc converter," *IEEE Transactions on Magnetics*, vol. 39, no. 4, pp. 2057 – 2061, July 2003.

[3] C. Sullivan and S. Sanders, "Design of microfabricated transformers and inductors for high-frequency power conversion," *IEEE Transactions on Power Electronics*, vol. 11, no. 2, pp. 228 –238, Mar. 1996.

[4] T. O'Donnell, N. Wang, M. Brunet, S. Roy, A. Connell, J. Power, C. O'Mathuna, and P. McCloskey, "Thin film micro-transformers for future power conversion," in *IEEE Applied Power Electronics Conference and Exposition*, vol. 2, 2004, pp. 939 – 944 vol.2.

[5] S. Prabhakaran, Y. Sun, P. Dhagat, W. Li, and C. Sullivan, "Microfabricated V-groove power inductors for high-current low-voltage fast-transient dc-dc converters," in *IEEE Power Electronics Specialists Conference*, June 2005, pp. 1513 –1519.

[6] N. Wang, T. O'Donnell, S. Roy, P. McCloskey, and C. O'Mathuna, "Micro-inductors integrated on silicon for power supply on chip," *Journal of Magnetism and Magnetic Materials*, vol. 316, no. 2, pp. e233 – e237, 2007.

[7] T. O'Donnell, N. Wang, R. Meere, F. Rhen, S. Roy, D. O'Sullivan, and C. O'Mathuna, "Microfabricated inductors for 20 MHz dc-dc converters," in *IEEE Applied Power Electronics Conference and Exposition*, Feb. 2008, pp. 689 –693.

[8] J. T. DiBene, P. Morrow, C.-M. Park, H. W. Koertzen, P. Zou, F. Thenus, X. Li, S. W. Montgomery, E. Stanford, R. Fite, and P. Fischer, "A 400 amp fully integrated silicon voltage regulator with in-die magnetically coupled embedded inductors," in *IEEE Applied Power Electronics Conference and Exposition, Special Presentation*, Feb. 2010.

[9] P. Morrow, C.-M. Park, H. Koertzen, and J. DiBene, "Design and fabrication of on-chip coupled inductors integrated with magnetic material for voltage regulators," *IEEE Transactions on Magnetics*, vol. 47, no. 6, pp. 1678 –1686, June 2011.

[10] S. Bae, Y.-K. Hong, J.-J. Lee, J. Jalli, G. Abo, A. Lyle, B. Choi, and G. Donohoe, "High Q Ni-Zn-Cu ferrite inductor for on-chip power module," *IEEE Transactions on Magnetics*, vol. 45, no. 10, pp. 4773 –4776, Oct. 2009.

[11] D. Yao, C. Levey, and C. Sullivan, "Microfabricated V-groove power inductors using multilayer Co-Zr-O thin films for very-high-frequency dc-dc converters," in *IEEE Energy Conversion Congress and Exposition (ECCE)*, Sept. 2011, pp. 1845 –1852.

[12] M. Wang, J. Li, K. Ngo, and H. Xie, "A novel integrated power inductor in silicon substrate for ultra-compact power supplies," in *IEEE Applied Power Electronics Conference and Exposition (APEC)*, Feb. 2010, pp. 2036 –2041.

[13] S. Mathuna, T. O'Donnell, N. Wang, and K. Rinne, "Magnetics on silicon: an enabling technology for power supply on chip," *IEEE Transactions on Power Electronics*, vol. 20, no. 3, pp. 585 – 592, May. 2005.

[14] C. Sullivan, "Integrating magnetics for on-chip power: Challenges and opportunities," in *IEEE Custom Integrated Circuits Conference*, Sep. 2009, pp. 291 –298.

[15] C. Sullivan, W. Li, S. Prabhakaran, and S. Lu, "Design and fabrication of low-loss toroidal air-core inductors," in *IEEE Power Electronics Specialists Conference*, june 2007, pp. 1754 –1759.

[16] W. Liu, J. Suryanarayanan, J. Nath, S. Mohammadi, L. Katehi, and M. Steer, "Toroidal inductors for radio-frequency integrated circuits," *IEEE Transactions on Microwave Theory and Techniques*, vol. 52, no. 2, pp. 646 – 654, feb. 2004.

[17] L. Vandi, P. Andreani, E. Temporiti, E. Sacchi, I. Bietti, C. Ghezzi, and R. Castello, "A toroidal inductor integrated in a standard cmos process," *Analog Integrated Circuits and Signal Processing*, vol. 50, pp. 39–46, 2007, 10.1007/s10470-006-9153-y. [Online]. Available: http://dx.doi.org/10.1007/s10470-006-9153-y

[18] J. Phinney, J. Lang, and D. Perreault, "Multi-resonant microfabricated inductors and transformers," in *IEEE 35th Annual Power Electronics Specialists Conference (PESC)*, vol. 6, june 2004, pp. 4527 – 4536 Vol.6.

[19] J. Phinney, "Multi-resonant passive components for power conversion," *PhD Thesis, MIT*, May 2005.

[20] S. Tang, S. Hui, and H. S.-H. Chung, "Coreless planar printed-circuit-board (PCB) transformers-a fundamental concept for signal and energy transfer," *IEEE Transactions on Power Electronics*, vol. 15, no. 5, pp. 931 –941, sep 2000.

[21] S. Orlandi, B. Allongue, G. Blanchot, S. Buso, F. Faccio, C. Fuentes, M. Kayal, S. Michelis, and G. Spiazzi, "Optimization of shielded pcb air-core toroids for high efficiency dc-dc converters," in *IEEE Energy Conversion Congress and Exposition (ECCE)*, sept. 2009, pp. 2073 – 2080.

[22] T. Pan, A. Baldi, E. Davies-Venn, R. Drayton, and B. Ziaie, "Fabrication and modeling of silicon-embedded high q inductors," in *17th IEEE International Conference on Micro Electro Mechanical Systems (MEMS)*, 2004, pp. 809 – 812.

[23] V. Ermolov, T. Lindstrom, H. Nieminen, M. Olsson, M. Read, T. Ryhanen, S. Silanto, and S. Uhrberg, "Microreplicated RF toroidal inductor," *IEEE Transactions on Microwave Theory and Techniques.*, vol. 52, no. 1, pp. 29 – 37, jan. 2004.

[24] X. Yu, M. Kim, F. Herrault, C.-H. Ji, J. Kim, and M. Allen, "Silicon-embedded 3D toroidal air-core inductor with through-wafer interconnect for on-chip integration," in *IEEE International Conference on Micro Electro Mechanical Systems (MEMS)*, feb. 2012, pp. 325–328.

[25] P. Hammond, *Energy Methods in Electromagnetism*. Oxford Science Publications, 1981.

[26] R. P. Sylvester and R. L. Ferrari, *Finite Elements for Electrical Engineers*. Cambridge University Press, 1983.

[27] M. Tolikas, J. Lang, and J. Kirtley, J.L., "Algebraic dual-energy thermal analysis with application to variable reluctance motor design," *IEEE IAS Annual Meeting*, pp. 736 –744, oct 1996.

[28] M. Tolikas, J. Lang, and J. Kirtley, "Algebraic dual energy magnetic analysis with application to variable reluctance motor design," *IEEE Transactions on Energy Conversion*, vol. 14, no. 3, pp. 270 –276, sep 1999.

[29] Maplesoft, "Maple," 2011, 15. [Online]. Available: http://www.maplesoft.com/products/maple/

[30] MathWorks, "Matlab," 2010, 7.11. [Online]. Available: http://www.mathworks.com/products/matlab/

[31] H. Woodson and J. Melcher, *Electromechanical Dynamics, Vol2*. John Wiley, 1968.

[32] J. R. Melcher, *Continuum Electromechanics*. MIT Press, 1981.

[33] M. Zahn, *Electromagnetic Field Theory*. Krieger Publishing Company, 1979.

[34] W. Ramo and V. Duzer, *Fields and Waves in Communication Electronics*. John Wiley, 1965.

[35] A. Agarwal and J. H. Lang, *Foundations of Analog and Digital Circuits*. Morgan Kaufman, 2005.

[36] J. Kim, F. Herrault, X. Yu, M. Kim, and M. Allen, "Microfabrication of air core power inductors with metal-encapsulated polymer vias," *Journal of Micromechanics and Microengineering*, Unpublished.